Chemical Engineering Science 296 (2024) 120214

Contents lists available at ScienceDirect

Chemical Engineering Science

journal homepage: www.elsevier.com/locate/ces

Plugging of pipes by cohesive particles. Computed tomography investigation and theoretical analysis

Boris V. Balakin [a,*], Yu-Fen Chang [a,b], Mona Øynes [a], Pavel G. Struchalin [a]

[a] Høgskulen på Vestlandet, Bergen, Norway
[b] Arctic University of Norway, Tromsø, Norway

ARTICLE INFO

Keywords:
Ice slurry
Clogging
Plugging
Computed tomography
Flow loop
CFD

ABSTRACT

Flow regimes leading to clogging of pipes exist for most multiphase flows with cohesive particles. Although plugging is critical in many industrial and medical applications, there are few records describing the details of the process. To address the problem, we conduct a computed tomography (CT) study of plugging in a cohesive ice slurry. We run experiments for ice concentration of 15%, Re∼3500, particle size 0.2-0.4 mm, and their surface energy ∼150 mJ/m^2. The CT scans, combined with experimental logs of the main flow parameters, revealed the formation of deposits around the orifice inserted into the pipe, with a complete blockage formed downflow the orifice. The deposition efficiency of ice was relatively low ∼ 10^{-3}. Reproducing the experimental deposition efficiency with the Lagrangian CFD model, we extracted the probability of particle capture at the orifice, which was about 0.5%. The simulation results illustrated how inter-particle interactions hindered the plugging.

1. Introduction

Clogging of flow channels by sticky particles is a phenomenon observed in daily life. The process constitutes multiple problems in chemical engineering: crystallizers (Shuainan et al., 2024), packed beds (Natsui et al., 2012), hydrate (Song et al., 2017; Kakitani et al., 2019), and ice slurries (Kauffeld et al., 2005; Onokoko et al., 2018) are subject to plugging in a variety of flow regimes. Despite the apparent simplicity of the process where particles stick together into a flow-stopping "snowball", important physical questions are hidden behind this simpleness. A particle-laden flow accelerates in an unblocked part of the cross-section. How does this affect the cohesive interactions of particles? Will this lead to particulate erosion or hydrodynamic breakage of the partially formed deposit? What is the role of local flow restrictions (e.g., bends or valves)? Do they promote or hinder the process of plugging?

Although mechanisms of particle re-suspension in turbulent flows are well explored and documented, (Henry et al., 2023; Ziskind, 2006), considering effects of adhesion, surface roughness, and granular interactions, it is still not entirely clear how the re-suspension coheres with the deposition of particles, often agglomerated and undergoing cohesive interactions with the deposit. Flow maps of multiphase flow regimes help characterize the phenomenon's complexity in simpler terms of structural taxonomy. Doron and Barnea (1996) developed flow regime maps based on numerical simulations for inertial sand particles in horizontal pipes. The particles were not cohesive, so the pipe's blockage was detected at particle volume fractions of about 50%, which was relatively close to their packing limit. Poloski et al. (2009) conducted a comprehensive experimental study that considered flow regimes in non-Newtonian glass, metal oxides, and cohesive kaolin clay slurries. They found that particles blocked the pipe at a particle volume fraction above 25%. The influence of flow restrictions and cohesion was illustrated by Hirochi et al. (2002), and Struchalin et al. (2023). They studied how an orifice promoted the formation of plugs in horizontal pipes with aqueous (Hirochi et al., 2002) and hydrocarbon-based (Struchalin et al., 2023) slurries of ice. As presented in the rheological investigation by Rensing et al. (2011), and noted by Kauffeld et al. (2005), the hydrocarbon-based slurries are more cohesive and prone to plugging. This is indirectly confirmed by comparing results from (Hirochi et al., 2002) and Struchalin et al. (2023) where the aqueous system was plugged when the limiting volume fraction was more than twice higher. Another experiment by Struchalin and Balakin (2023) demonstrated how the flow restrictions promoted plugging: blind T-junctions and other dead ends of the flow channel accumulated deposits upflow the orifice. Similar observations were obtained by Santo and Kalman (2017). In Struchalin and Balakin (2023), the deposits were re-dispersed

* Corresponding author.
E-mail address: Boris.Balakin@hvl.no (B.V. Balakin).

https://doi.org/10.1016/j.ces.2024.120214
Received 26 February 2024; Received in revised form 15 April 2024; Accepted 2 May 2024
Available online 9 May 2024

back into the flow as massive slugs that finally blocked the orifice. Although experimental logs were provided for the main flow parameters (Struchalin et al., 2023; Hirochi et al., 2002), none of the abovementioned works quantified detailed dynamics of the deposit formation. They did not depict how the deposit converted to a plug.

As a fruitful alternative to the flow regime classification, during the past three decades, non-contact densitometry and tomography of slurries became a powerful experimental tool (Silva, 2022). These methods enable a non-invasive control of the multiphase flow patterns for a transient process. However, most of the existent measurement techniques (electric, magnetic) are limited by the type of the considered dispersed phase, which must not interact with the scanning field. When radiation safety is ensured, gamma-ray methods can go beyond the limitations and provide detailed information on concentration and velocity profiles (Heindel, 2011). There are records of numerous gamma-ray studies of gas-solid and gas-liquid flows (Heindel, 2011), while the number of works on slurries could be much higher. Gillies with co-workers (Gillies et al., 1999, 2000) studied the hydro transport of non-cohesive sand by glycol in an experimental flow loop equipped with a gamma-densitometer. The flow velocity was in the interval 0.014-4 m/s, the bulk concentration of the particles was up to 20%, and the sand grains' size was 430 μm. George et al. (2001) conducted a combined study applying gamma-ray and electrical impedance tomography to a three-phase system. A flow of water, air, polystyrene, and glass particles was depicted in a massive vertical pipe with a diameter of 19.5 cm. The flow velocity was in the interval 0.29-2.90 m/s, the bulk concentration of particles was up to 30%, and the particles' size was between 40 and 700 μm. Kaushal and Tomita (2007) conducted a similar experiment for a water-based slurry with 400- μm sand particles, altering mean flow velocity (1-5 m/s) and the concentration of particles (up to 50%). The dispersed phase concentration profile was measured by a sampling probe, the measurement of which was verified by a gamma-ray densitometer. The accuracy of the gamma-ray method was higher for the case with significant deposition of sand particles where iso-kinetic sampling was not possible. The densitometry revealed the existence of a local maximum particle concentration apart from the walls. Krupička and Matoušek (2014) conducted a gamma-ray tomographic study of a slurry consistent with water and glass beads. The mean flow velocity was in the interval 2-4 m/s, and the maximum size of the particles was 1.5 mm. Particle concentration profiles were obtained for heterogeneous flow regimes with the maximum bed concentration of 60%. The experiments aimed to produce a high-quality benchmark for validating numerical models. Hashemi et al. (2021), who studied a cohesive clay slurry applying gamma-ray and electrical resistance tomography, expressed a similar motivation. The experiments were carried out for particle concentrations up to 30%, and the size of the particles was between 100 and 280 μm. The mean flow velocity was in the interval 0.5-2.0 m/s. The dual-sensor method resulted in high-resolution snapshots of particle concentration for different flow regimes. The pipe clogging was not depicted in the discussed tomographic studies.

Numerical simulations of the phenomenon could provide a detailed physical insight into the problem. Although the numerical simulation of plugging is limited due to the incompleteness of physical closures and high computational costs, significant progress has been made in the multiphase CFD of deposition. Eulerian multiphase CFD models for blockage by asphaltenes (Eskin et al., 2011), gas hydrates (Balakin et al., 2011), and blood clots (Rukhlenko et al., 2015) were capable of simulation the formation of deposits. Models based on the Eulerian multiphase approach produced continuous deposits that hindered the flow due to a cross-section reduction (Balakin et al., 2011). This contradicted experimental evidence on the formation of discrete flow obstructions (Struchalin et al., 2023; Hirochi et al., 2002). The Eulerian models were based on empirical correlations with fitting parameters. To improve the precision of simulations, Lagrangian CFD-DEM models were developed to simulate cohesive interactions during the contact of individual particles and walls of the channel (Mondal et al., 2016; Duan et al., 2021). The simulations succeeded in reproducing realistic shapes of plugs in flow restrictions and pores (Yang et al., 2019). The plugs intercepted the dispersed phase but were not optimally coupled with the continuous phase, as they did not lead to a reduction of the flow rate. Very few numerical models of plugs were validated against experiments. Recently, Saparbayeva and Balakin (2023) reported a CFD-DEM model reproducing experiments on plugging in the ice-decane slurry (Struchalin et al., 2023). The model demonstrated how the cohesion of particles influenced the dynamics of plugging. In addition, it was computationally shown that sticky particles from the bulk of the flow scrubbed the surface of deposits and then re-suspended the settled particles. Although the model provided significant insight into the physics of plugging, the computational costs of the method limited simulation to a two-dimensional geometry and thus reduced the physical realism of the simulations.

Concluding the overview, we note that different aspects of plugging in cohesive slurries have been recently considered in the FLOWCHART project (Research Council of Norway, 2024). Previous works focused on flow maps and assessment of plugging risks (Struchalin et al., 2023), the influence of local flow restrictions (Struchalin and Balakin, 2023), rheology of the slurry (Naukanova et al., 2023), and CFD-DEM modeling of plugging (Saparbayeva and Balakin, 2023). In this paper, we focus on details of plug formation and thus run plugging experiments controlled by medical computed tomography to elucidate the process of plugging using CT scans. We analyze the kinetics of the process and deduce the deposition efficiency. Further, we develop a computationally inexpensive CFD model to match and interpret the experimental observations. We discuss the plugging mechanisms and support our conclusions with the numerical results and simplified theoretical estimates.

2. Experiments

The experiments focused on plugging in a slurry of ice particles dispersed in decane. The plugging was induced by an orifice installed in the test section of a multiphase flow loop. As follows from Yang et al. (2004) and Döppenschmidt et al. (1998), in this system, the ice particles are sticky due to a liquid layer formed at the ice surface. The layer forms capillary bridges when the ice particles interact. The classical van-der-Waals interaction occurs when the deposited particles are in close contact. The combination of both attractive mechanisms is termed as "cohesion" below.

2.1. Experimental flow loop

The test section was placed inside the CT scanner and periodically subjected to scanning upon the complete stop of the flow due to the plugging. Scanning the test section, we tracked how the deposit evolved until it became the plug. To avoid imaging artifacts due to metallic inclusions, the scanned part of the test section was made of borosilicate glass (∅30×4 mm). The glass pipe was glued into the 3D-printed plastic (PLA) adaptors with flanges. The orifice is also made of the same plastic. The glass pipe is a part of the horizontal section fixed on a patient bed of the CT scanner. The total length of the horizontal pipe is 1.73 m. The orifice was installed 85 cm from the inlet to the test section, corresponding to 38.6 hydraulic diameters. The horizontal section was connected to the rest of the loop with two 90-degree T-junctions using flexible fuel-grade hoses. The internal surface of the hoses is covered by smooth nitrile rubber. The hoses were connected to the rest of the loop through flanges. This allowed for maintaining the mobility of the patient bed and scanning the entire glass pipe. The experimental set-up mounted in the scanner is presented in Fig. 2.

The flow loop is equipped with thermal and pressure sensors. In this modification of the flow loop, we removed the Coriolis flow meter as, according to previous experience, it influenced the plugging. We performed a virtual flow metering instead (Amin, 2015). The specification of the measurement system is presented in Table 1. The sensor signals

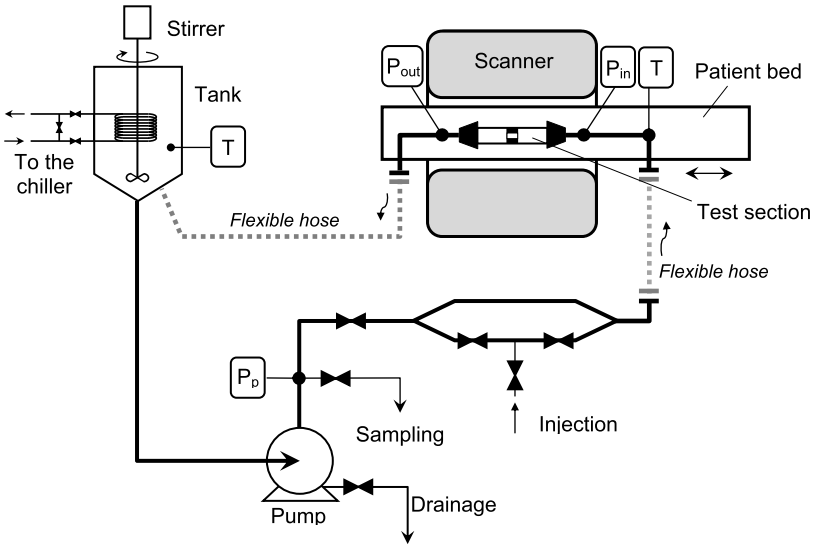

Fig. 1. Scheme of the set-up.

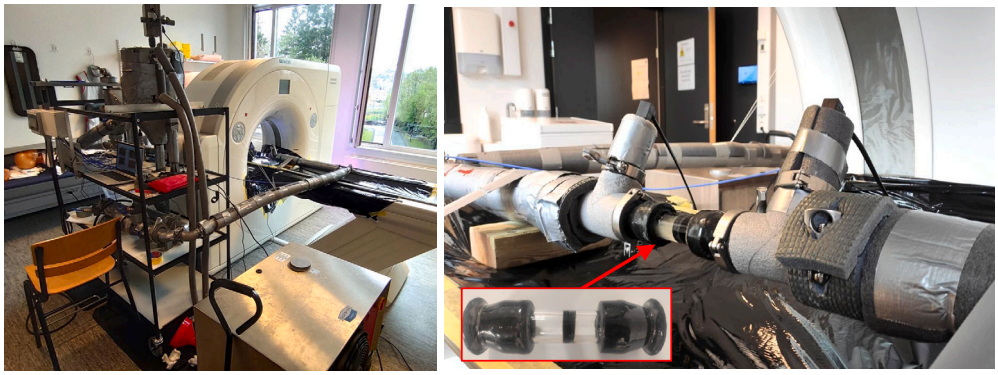

Fig. 2. The flow loop and the CT scanner (left), the test section (right).

Table 1
Measurement system.

Parameter	Sensor	Range	Error
Temperature	PT100 + LKM 103 Transducer	-40~85 °C	±0.1 °C
Pressure difference	Gems 3500 Pressure Transmitter	0~4 bar	0.25%
Pressure	Omega PXM219-006AI	0~6 bar	0.25%

were collected and processed using the National Instrument 6001 DAQ USB data card operated under a LabView-based control program with an acquisition frequency of 1 kHz. (See Fig. 1.)

A 2.2-kW centrifugal pump from Pedrollo delivered the slurry from the expansion tank. The ABB ACS355 frequency converter controlled the speed of the pump. The expansion tank contained a heat exchanger and a temperature sensor to maintain the required temperature of the slurry. The heat exchanger had a bypass line with the valve system to vary the cooling capacity. It was connected to the external chiller (WTG-Quantor Chilly 25 M-LT). The tank was also equipped with a continuously operated stirrer (Joanlab OSC-20L) with a 75-mm three-blade impeller to keep the homogeneity of the slurry. Two layers of polyethylene foam thermally insulated the entire outer surface of the flow loop. The average thermal resistance of the walls was 5.3 (m^2·K)/W.

2.2. Experimental procedure

A routine experimental procedure is as follows. Knowing the required concentration of particles (15% vol.) and the total volume of slurry required for the experiment (25.7 *l* ± 3%), two separate volumes are prepared to contain pure decane and a high-concentrated mixture of decane with ice particles (19~20% vol.). The mixture is made by crushing ice cubes in decane using a BN750EU mixer from Ninja. Slurry production was done in a freezer at -22 °C. Then, the slurry was collected in a tank and stored at -22 °C before charging into the loop. As a result, the fresh slurry has particles with a diameter from 0.2 to 0.4 mm. The granulometric analysis of the particles is described in Struchalin et al. (2023). Resulting particle size distribution for the freshly produced slurry and in-situ samples from the system are presented in Fig. 3. These data are supplemented with particle size distributions by Naukanova et al. (2023) who measured the apparent viscosity of the slurry.

Before the experiments, the flow loop was pre-conditioned by charging 9 l of pure cold decane with a temperature of -22 °C. Then, the temperature of the walls became negative, and the decane-ice mixture was loaded into the loop. During this procedure, the pump frequency increased gradually from 20 to 30.6 Hz, and the stirrer accelerated from 1200 to 2000 rpm. The chiller was used to maintain the temperature in the tank. The described sequence of charging ensures the homogeneity of the slurry and protects the system from cavitation.

After the charging procedure, the temperature of the slurry was in the range of -6~-8 °C. Next, the slurry was thermally stabilized at -1.7~-1.6 °C, which gave ~ -1 °C at the test section inlet at the desired in the experiment flow rate. When the thermal stabilization was done, the pump frequency was reduced to 7 Hz, and the plugging started. This has to be noted that positive temperatures could be set locally in the rig. There were two places where local heating was possible:

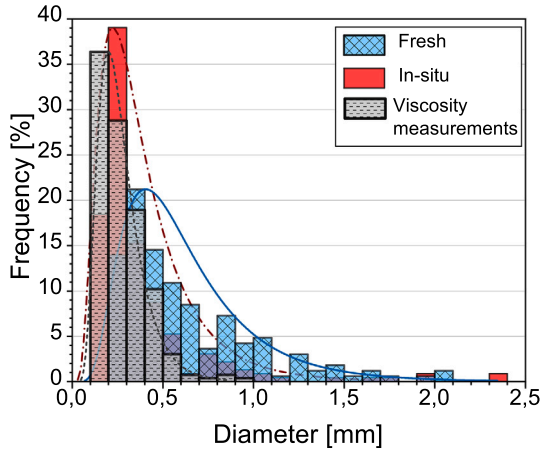

Fig. 3. Particle size distribution in the ice slurry. Freshly produced slurry (fresh) compared with the results of in-situ sampling (Struchalin et al., 2023) and the measurements conducted during rheological investigation (viscosity measurements) by Naukanova et al. (2023).

Table 2
Experimental conditions.

No.	Type	Particle conc., % vol.	Tank temp., C	Flow rate, kg/h
1	CT	15	−1.7	259
2	CT	15	−1.6	284
3	CT	15	−1.8	339
4	Lab	15	−1.7	328
5	Lab	15	−1.8	318
6	Lab	15	−1.6	323
7	Lab	15	−1.7	294

the non-insulated test section and the pump. It was likely that partial melting took place in the pump. However, the temperature was restored in the cooling tank, where particle residence time is longer than in the pump by an order of magnitude. After the pump, the particles were directed to the test section via the thermally insulated piping within a very short time comparable to the thermal response time of the particle. The temperature was always negative in the test section as no melting of the deposits was observed for an entire experiment.

The main parameters of experiments are summarized in Table 2.

2.3. Computed tomography

The test section was scanned in a Siemens Somatom Perspective CT scanner (Siemens, 2019). The X-ray tube and the detector array of 32 detector rows are sited on opposite sides of each other in the gantry of the scanner (Siemens, 2019). The test section was scanned with the helical scan mode placed on a table, continuously moving through the gantry, while the X-ray tube and the detector array rotated continuously. Multiple projection data were collected during the rotation, and the filtered back-projection technique reconstructed axial image slices. The pitch, i.e., the ratio between table distance traveled per rotation and collimation (beam width) (Seeram, 2009), was 0.55. This small pitch gives more overlap of the X-ray beam irradiating the object and longer scan time than for settings with higher pitch factors. The quality of the image reconstruction is improved in this way. Choosing the maximum collimation and the minimum rotation time of 0.6 s ensured a short scan time in the experiment. The collimation was 19.2 mm (Siemens, 2019). To ensure a high signal-to-noise ratio (SNR) for the images, the test section was scanned using the automatic tube current modulation (ATCM) with a quality reference of 220 mAs. The mean effective setting was 62 mAs when scanning the test section, and given the values of pitch and rotation time, this corresponded to a tube current of about 57 mA. To maximize the contrast between decane and ice, the lowest tube voltage for the scanner, 80 kV, was chosen.

Table 3
Settings of the CT scanner.

Protocol	HeadRoutine (Adult)
Topogram	Lateral
Scan direction	Caudocranial
Scan type	Helical
Scan time	7.82 s
Rotation time	0.60 s
Pitch	0.55
Collimation	32x0.6 mm
Quality reference mAs	220 mAs
Effective mAs	62 mAs
Tube voltage	80 kV
Display field of view	50 mm
Window settings	width 1200 HU, level -600 (Lung)
Reconstruction kernel	H31s medium smooth+, H45s medium+
Slice thickness/recon increment	0.6 mm/0.6 mm, 1 mm/1 mm, 2 mm/2 mm, 5 mm/5 mm

The matrix size of the axial images is 512 x 512 pixels (Siemens, 2019). Using a display field of view of 50 mm when reconstructing the images resulted in a pixel size of approximately 0.1 mm x 0.1 mm for the axial slice images of the test section. The helical scan mode also provided volumetric image data with a voxel size of approximately 0.1 mm x 0.1 mm x slice thickness. The minimum slice thickness was 0.6, determined by the detector size (Siemens, 2019). After calibration measurements, the “Lung window” was chosen as the best representation of the width/window level setting. The images were also reconstructed with a softer reconstruction filter, H31s medium smooth+, for improved SNR, and a sharper filter, H45s medium+, for enhanced spatial resolution. An overview of the settings, scan parameters, and reconstruction parameters used in the scanner‘s digital interface are provided in Table 3.

2.4. Computed tomography image acquisition and processing

The CT scanner acquired a stack of DICOM images in each acquisition. The images were subsequently imported into the Fiji software (Schneider et al., 2012; Schindelin et al., 2012). The alignment between the stacks was achieved through a meticulous comparison of distinctive features among different stacks. This critical step ensures accurate spatial alignment for further analysis. Once aligned, uniform parameters such as contrast and color map settings are applied consistently across all image stacks within a given experiment. This standardization ensures a reliable and consistent basis for subsequent analysis and interpretation. The 3D CT image sequence is then subjected to a thresholding method to identify pixels exceeding a predefined threshold. In this particular case, the “Shanbhag” thresholding method (Shanbhag, 1994) was chosen, considering the irregular nature of the ice network under investigation. The thresholded pixel data obtained from this process are subsequently utilized for the subtraction of the pipe, allowing for the precise isolation of the ice structure.

2.5. Virtual flow metering

The mass flow rate of the slurry was computed by combining two measurements: the differential pressure in the test section and the geometry of the settled deposits obtained using the CT. The test section was split into three zones: the uplow part before the orifice, the orifice, and the downflow part after the orifice. For each CT snapshot, the size of the deposit was determined. Then, the equivalent hydraulic diameter of the parts D_i was computed, accounting for the partial blockage of the cross-section by ice deposits. Next, the following iterative procedure was applied:

1. an initial value of the mass flow is assumed, and the mean flow velocity in a given part u_i is determined;
2. using the known data on the concentration ϕ_p, size d_p, and cohesion of particles F_c, the density ρ_{mix} and the apparent viscosity of the slurry $\mu_{s,i}$ are calculated using the procedure from (Struchalin et al., 2023; Naukanova et al., 2023). Here we iterated updating the share rate to converge the apparent viscosity;
3. the flow resistance and the friction coefficient for a part are determined as ξ_i and λ_i using empirical expressions from Idelchik (2008); $Re_i = \rho_{mix} u_i D_i / \mu_{s,i}$ with the apparent viscosity dependent on u_i;
4. the total pressure drop is computed as $\Delta p = 1/2 \rho_{mix} \Sigma(\delta_{i,0}\xi_0 + \lambda_i L_i / D_i) u_i^2$, where L_i is the length of the part and $\delta_{i,0}$ is the Kronecker delta. The pressure drop is further compared with the experimental value;
5. next iteration corrects the mass flow rate in p.1 until the discrepancy with the experiment falls below the controlled value. The total number of iterations until the convergence was from 5 to 7.

A complete description of the method is cumbersome and thus presented in the Supplementary Materials. The virtual flowmetry we applied was verified against experiments controlled by a Coriolis flowmeter. The verification is illustrated in the Supplementary Materials. The discrepancy was from 5% to 25% where the maximum deviation was observed at the final moments of plugging.

2.6. CFD simulations

We further present a CFD model developed to facilitate a theoretical analysis of the experimental results. The model is used to quantify how the interactions between particles, fluid, and walls influence particle deposition efficiency in the test section. The model is based on the Eulerian-Lagrangian principle (Crowe et al., 1998). The flow of decane is modeled using Navier-Stokes equations (Zhou et al., 2010; Siemens Digital Industries Software, 2020):

$$\frac{\partial \phi_l \rho_l}{\partial t} + \nabla \left(\rho_l \phi_l \vec{u} \right) = 0; \tag{1}$$

$$\frac{\partial \left(\rho_l \phi_l \vec{u} \right)}{\partial t} + \nabla \left(\rho_l \phi_l \vec{u}\vec{u} \right) = -\phi_l \nabla p + \phi_l (\mu_a + \mu^t) \nabla^2 \vec{u} + \phi \rho_l \vec{g} - \vec{F}_p, \tag{2}$$

where $\vec{g}$ is the acceleration due to gravity, ϕ_l is the volume fraction of decane, $\vec{u}$ is the velocity of decane, ρ_l is the density of decane, and p is the pressure. To account for the energy dissipation due to particulate collisions, we replaced the viscosity of decane μ_l with a polynomial fit of experimental values for the apparent viscosity of the slurry $\mu_a = \mu_l \left(1.0 - 0.4\phi_p + 49.5\phi_p^2 \right)$ (Struchalin et al., 2023), where $\phi_p = 1\text{-}\phi_l$ is the volume fraction of ice. The turbulent viscosity μ_t is computed using the standard k-epsilon turbulent model (Siemens Digital Industries Software, 2020). An isothermal flow is assumed. The inter-phase momentum coupling term is given by the superposition of drag and lift forces acting on particles from a computational cell $\vec{F}_p = \Sigma \left(\vec{f}_{d,i} + \vec{f}_{l,i} \right) / v_c$, where v_c is the volume of the cell.

The linear motion of the ith particle is governed by Newtonian mechanics (Zhou et al., 2010):

$$m_i \frac{\mathrm{d}\vec{v_i}}{\mathrm{d}t} = \vec{f}_{d,i} + \vec{f}_{l,i} + m_i \vec{g} - (m_i / \rho_p) \nabla p + \vec{f}_{s,i}, \tag{3}$$

where m_i is the mass of the particle, $\overline{v_i}$ is the Reynolds-averaged velocity of particles, ρ_p is the density of the particle. The rotational motion of particles is resolved similarly where torques of the particle forces are computed. The phases are two-way coupled via the continuity and momentum equations where the drag and the lift forces are the main drivers of the inter-phase momentum transfer. The particle and the fluid solvers are coupled using the standard iterative method described in Crowe et al. (1998).

The drag force is computed as (Crowe et al., 1998):

$$\vec{f}_{d,i} = (\pi/8)\, d_{p,i}^2 C_{D,i} \rho_l (\vec{u} - \vec{v}_i) |\vec{u} - \vec{v}_i|, \tag{4}$$

where $d_{p,i}$ is the particle size. In the simulations, we used an average value from the experimental interval $d_{p,i} = 300$ μm.

The drag coefficient is calculated to account for the presence of multiple particles in a computational cell using the expression by Di Felice (Di Felice, 1994):

$$C_{D,i} = \left(0.63 + \frac{4.8}{\sqrt{\phi_l Re_{p,i}}} \right)^2 \phi_l^{2-\overline{\xi_i}}, \tag{5}$$

where $Re_{p,i} = \rho_l |\vec{u} - \vec{v}_i| d_{p,i} / \mu_l$.

$$\overline{\xi_i} = 3.7 - 0.65 \exp\{-0.5 \left(1.5 - \log[\phi_l Re_{p,i}] \right)^2\} \tag{6}$$

The drag coefficient is introduced in the code using the field function.

The lift force f_l is given as Crowe et al. (1998):

$$\vec{f}_{l,i} = c_{l,i} \rho_l (\pi/8)\, d_{p,i}^3 \left(\vec{u} - \vec{v}_i \right) \times \vec{\omega}, \tag{7}$$

where $\vec{\omega} = \bigtriangledown \times \vec{u}$ is the curl of the fluid velocity.

The lift coefficient c_l is calculated using Sommerfeld's expression (Sommerfeld et al., 2000):

$$c_{l,i} = \frac{4.1126}{\mathrm{Re}_{s,i}^{0.5}} f_i \left(\mathrm{Re}_{p,i}, \mathrm{Re}_{s,i} \right), \tag{8}$$

where $\mathrm{Re}_{s,i} = \rho_l d_{p,i}^2 |\vec{\omega}| / \mu_l$ is the Reynolds number for shear flow, and function f is given as:

$$f_i = \begin{cases} \left(1 - 0.3314\beta^{0.5} \right) e^{-0.1\mathrm{Re}_{p,i}} + 0.3314\beta^{0.5} & \mathrm{Re}_{p,i} \le 40 \\ 0.0524 \left(\beta \mathrm{Re}_{p,i} \right)^{0.5} & \mathrm{Re}_{p,i} > 40, \end{cases} \tag{9}$$

$\beta = 0.5\mathrm{Re}_{s,i} / \mathrm{Re}_{p,i}$.

The interphase momentum transfer terms are computed with the particle velocity corrected by turbulent fluctuations $\vec{v}_i = \overline{\vec{v}_i} + \vec{v}^t$. The turbulent fluctuation velocity $\vec{v}^t$ is a random number taken from a zero-mean Gaussian distribution with a standard deviation $\sim\sqrt{(2/3)k}$ with the turbulent kinetic energy k (Siemens Digital Industries Software, 2020). The fluctuation velocity is added to the average velocity within the eddy interaction time (Gosman and Ioannides, 1983).

To model a dense multiphase system at a reasonable computational cost yet to account for inter-particle collisions, we implement a solid-pressure force derived from Bouillard et al. (1989):

$$\vec{f}_{s,i} = -\phi_p \nabla \phi_p \exp\{-K \left(\phi_{max} - \phi_p \right)\} / N \tag{10}$$

where $\phi_{max} = 0.56$ (Struchalin et al., 2023) is the conservative estimate of the packing limit, N is the number of particles in a computational cell, and K is the compaction modulus. Supplementary simulations of a single ice particle settling in decane to a bed of particles packed to ϕ_{max} were carried out to identify that the particle rebounded from the bed at $K = 100$. This value was further used in the simulations. The solid pressure force is introduced to the code using the field function.

The CFD-model is based on the Lagrangian routine available in STAR-CCM+ from Siemens, where custom expressions for the drag force f_d, the solid pressure f_s force, and the rheology of the slurry μ_a are introduced using field functions. We used the standard approach available in the code for the collisions of particles with the walls. During the collisions, the particles stick to the walls with a given probability p_w (Siemens Digital Industries Software, 2020). The code chooses a random number of particles colliding with walls using a uniform probability distribution in the range $[0, p_w]$ and assigns their post-collisional velocity to zero. The rest of the colliding particles with $p_w = 0$ follow the hard-sphere model (Crowe et al., 1998; Siemens Digital Industries Software, 2020), scaling the normal and the tangential components of the pre-

Table 4
Parameters used in the CFD model and theoretical calculations.

mass flow rate	275 kg/h
particle concentration ϕ_p	0.15
mass flow rate	275 kg/h
diameter of particles d_i	300 μm
density of fluid ρ	747 kg/m^3
density of particles ρ_p	916 kg/m^3
fluid viscosity μ	1.29 mPa·s
coefficients of restitution	$\epsilon_n = 0.6$, $\epsilon_\tau = 0.8$
packing limit ϕ_{max}	0.56
compaction modulus K	100
wall capture probability (CFD) p_w	0.4~100%
Young's modulus ice	2.4 GPa
Poisson's ratio ice	0.3
surface energy σ_c	150 mJ/m^2

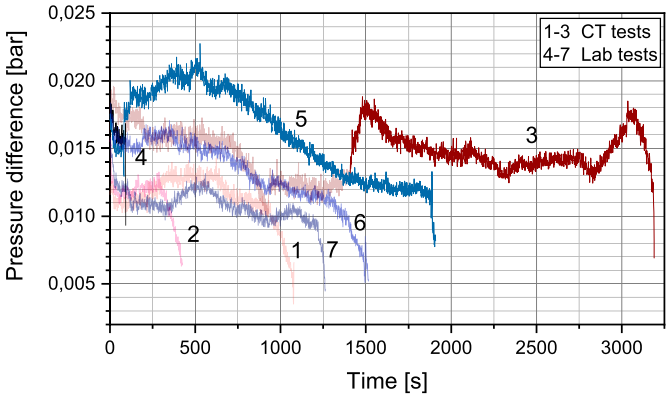

Fig. 4. Pressure drop as a function of time.

collisional velocity by respective restitution coefficients: $\epsilon_n = 0.6$ and $\epsilon_\tau = 0.8$ as in Saparbayeva and Balakin (2023).

The geometry of the CFD-model replicates the actual geometry of the experimental test section and the orifice. The geometry is discretized by 1-mm polyhedral cells with 0.3-mm prismatic near-wall refinement to obtain Y+ < 1. The mesh was defined using the standard grid independence study. The end boundaries of the model include a prescribed velocity inlet and a pressure outlet. The no-slip walls with standard wall functions are used. The particles were injected into the flow after stabilizing the continuous phase velocity profile. SIMPLE (Siemens Digital Industries Software, 2020) was used to solve the governing equations. The relaxation coefficients were 0.2 pressure, 0.8 velocity, and 0.8 turbulence model. The spatial discretization was done using the upwind scheme, and the temporal discretization was done after the implicit Euler scheme with a time step of 5 ms. Before multiphase simulations were carried out, the model had been validated using the experimental pressure drop measurement in the text section. The validation, illustrated graphically in the Supplementary Materials, revealed an average discrepancy of 9%.

3. Results and discussion

3.1. Experimental logs

Before the CT-controlled experiments, we conducted four runs of the flow loop outside the CT scanner. Then, three independent runs were performed in the scanner. Fig. 4 presents the pressure drop history. The results of the mass flow metering for the CT-based cases are presented in Fig. 5. In addition, we provide separate experimental logs for the CT-controlled experiments combining measured and computed parameters in a single plot in the Supplementary Materials. As follows from the figure, a significant spread of the time required for the blockage of the system was detected. This parameter was in the interval 100~3400 s.

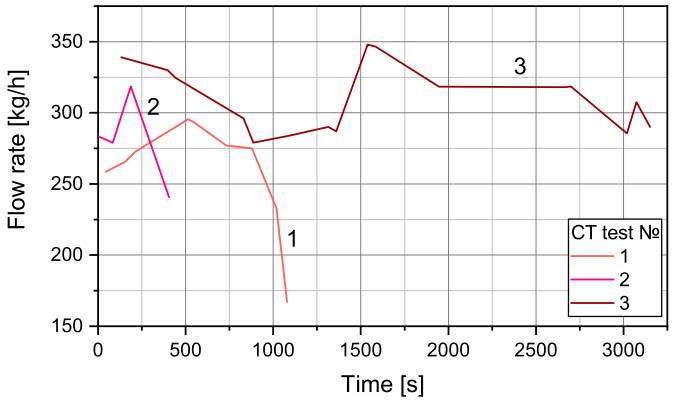

Fig. 5. Computed mass flow rate as a function of time.

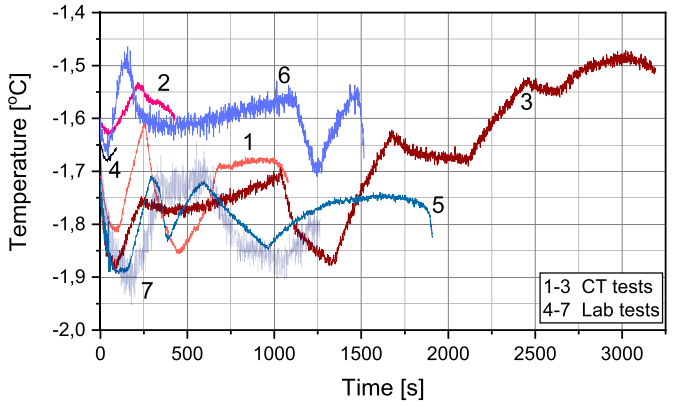

Fig. 6. Experimental temperature logs.

The peak pressure drop values were in the interval 0.12~0.22 bar, and the maximum mass flow rate was computed as 350 kg/h. Based on the previous experience (Struchalin et al., 2023), we identify three process conditions responsible for the spread. A partial pump blockage occurred in experiments 2 and 4; the flow stopped faster than in the cases with the pipe blockage. Cases 1 and 7 started at the comparable flow rate of ~260 kg/h. However, following Fig. 6(left) with experimental temperature logs, cases 1 and 7 ran at different temperatures with the initial peak values -1.95 to -1.70 ^{0}C. According to Yang et al. (2004) and Struchalin et al. (2023), the cohesive forces differ in this interval. The third group consists of experiments 3, 5, and 6, where the flow rate was ~30% elevated relative to cases 1 and 7. In these cases, better dispersion of particles is expected due to the enhanced inter-phase momentum transfer. Cases 3,5,6 differ by the initial temperature setting and the magnitude of the initial flow rate.

3.2. CT scans

For the CT-controlled experiments, we additionally present logs of the mass flow rate in Fig. 5 and the deposit-free diameters of the test section in Fig. 7. The diameters are averaged over distances equal to two main pipe calibers from the orifice. Information about the thickness of the deposit was obtained from the longitudinal vertical axial cross-section of the 3D CT images. These pictures are also shown in Figs. 8–11. All three CT-controlled experiments ended with blockages.

As seen in Fig. 8, the behavior of ice accumulation at the front and the back of the orifice is different in the early stages. At the frontal part of the orifice, the ice is halted by the walls of the orifice. Particle's Stokes number in the laminar layer around the walls is ~0.12, so they engage in an inertial deposition scenario. The formation of the deposits leads to a 20-30% increase in the pressure drop at ~250, 500, and 1500

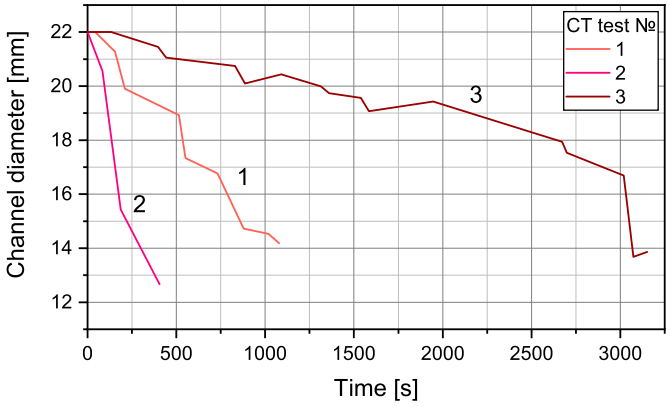

Fig. 7. Diameter of non-blocked cross-section as a function of time.

s for cases 2, 1, and 3, respectively. In Fig. 9, we observe that the formation of deposits in the frontal part of the orifice was asymmetric due to the prior history of the flow, which was bent before entering the test section. The deposits in the frontal part formed a sandwatch-like structure that streamlined the orifice yet narrowed the cross-section. This preserved the flow rate at a relatively constant level for up to ~80-90% of the process duration. The partial obstruction of the flow channel resulted in increased flow velocity in the plug-free regions, which reduced the apparent viscosity of ice slurry (Struchalin et al., 2023) and preserved the flow. The pressure drop also rolls back to 20% of the peak value at this stage. The deposition in the frontal part of the orifice does not result in the blockage of the entire cross-section.

A more uniform but shorter deposit forms after the orifice under the influence of the turbulent dispersion of particles. The ice is trapped in the stagnation zones where the orifice shades the main flow. This "tail" deposit radially grows from all directions until the average hydraulic diameter of the pipe falls to ~60% of the initial diameter. A far-field deposition occurs at about 2 pipe diameters on both sides of the orifice. This process is significantly slower and is caused by the gravitational settling of particles. Although not responsible for the blockage of the cross-section, the gravitational settling contributes to the final increase of the flow resistance and is thus attributed to the overall jamming of flow by deposits. Fig. 9 shows that the entire cross-section's blockage occurs in the test section's downflow part just after the orifice. The plug is relatively porous, with several voids in the central part of the pipe.

The tank temperature (Fig. 6) changes with plugging in the following manner: an initial increase due to the heat input during the ice loading procedure, then thermal stabilization of the flow. Temperature fluctuations after the initial stabilization are due to the automatic thermal regulation of the chiller. When the flow rate changes due to the formation of deposits, the heat transfer with the chiller and to the environment alters with a delay corresponding to the thermal response of the loop. Massive deposits of ice formed an extra layer of thermal insulation and thus limited the heat flux from the environment. At the end of the experiments, the temperature increased again in response to the progressive deposition and associated enhanced friction in the flow loop.

3.3. Deposition of particles

The deposition of particles is an obvious reason for the formation of plugs. The process can be quantitatively characterized using the so-termed deposition efficiency, representing the relative number of particles deposited in the process:

$$\eta = \frac{\phi_{p,in} - \phi_{p,out}}{\phi_{p,in}}, \tag{11}$$

where indices *in* and *out* denote the entrance and escape boundaries. This parameter is extracted from our data following the particle mass balance principle in the test section $dm_p/dt = \dot{m}_{in} - \dot{m}_{out}$. For an incompressible flow, a simple derivation leads to:

$$\eta = \frac{\tau_{res}}{\phi_{p,in}} \frac{d\phi_p}{dt}, \tag{12}$$

where τ_{res} is the particle residence time in the test section. An order-of-magnitude estimate of the deposition efficiency is presented in Fig. 14(left) as a function of time. To calculate η, we assumed that the most intensive deposition goes in the test section and the inlet concentration of particles $\phi_{p,in} \sim const$. The figure shows that the deposition efficiency is relatively low $\sim 10^{-3}$. The average deposition efficiency was 0.14% in the CT-controlled experiments. Although the parameter could be underestimated, the deposition of about half of the particles in the rest of the flow would not significantly alter the order of the parameter. The deposition efficiency tends to reduce with time in experiments CT-1 and CT-2. This is related to a better streamlining of the cross-section by deposited particles. In experiment CT-3, after a similar reduction at the first ~1500 s of the process, the deposition efficiency increased till the end of the experiment. To explain this difference, we refer to Fig. 6(left), which demonstrates a notable temperature increase in the second half of CT-3. The respective increase of the cohesion and the following deposition happens as expected.

Verifying the obtained results with the existing theoretical knowledge on deposition at an orifice is important. For this purpose, we utilize the expression by Muyshondt et al. (1996) developed for deposition in a turbulent orifice:

$$\eta = \{1 + \left(St\left(1 - D_0^2/D_1^2\right)/3.14\exp[-0.0185\theta]\right)^{-1.24}\}^{-1}, \tag{13}$$

where D_0, D_1 are the diameter of the orifice and the pipe where the orifice is installed (without deposits), St is the particle Stokes number in the bulk, and θ is the contraction half-angle of the orifice. For 300- μm particles, Eq. (13) returns $\eta = 75.1\%$, two orders greater than the experimental result.

The difference between the experiment and the theory is noticeable because just a few particles stick and remain in the test section. To estimate an average probability of particle capture in the test section, we assume that inertial deposition at vertical surfaces of the orifice is the dominant mechanism for their deposition. In this case, the mass flow of deposited particles is proportional to the total mass flow as $2p_w\dot{m}_{in}\left(D_1^2 - D_0^2\right)/D_1^2$. Then, making use of Eq. (11) and the mass balance, the probability becomes $p_w \sim 0.5\eta D_1^2/\left(D_1^2 - D_0^2\right) = (0.26 \pm 0.08)\%$. The deposition also happened in other parts of the test section. The CFD model was used to verify the coarse estimate of p_w.

First, we demonstrate the flow patterns predicted by the model. The simulations were carried out for up to 5 residence times of particles in the test section. Figs. 12-13 illustrates the velocity magnitude and the formation of deposits in the axial cross-section of the pipe. As follows from the plot, massive wakes are formed in the flow just after the orifice. As a result, as in the experiments, uniform deposits of particles are formed in the corners of the downflow part of the orifice. Inertial deposition happens in the frontal part of the orifice. The rheological expression contributes to particles' jamming of the flow, so the low-velocity zones are associated with the dense deposits. Particle slugs are formed when passing the orifice. The slugs' size correlates with the orifice's size and the frequency of their formation - with the length of the orifice and flow velocity. Due to the high computational costs and the different set of boundary conditions (Saparbayeva and Balakin, 2023), the model did not reproduce experiments entirely or simulate later stages of plugging.

In Fig. 14, we quantify the relation between the deposition efficiency and the probability of wall capture p_w. Reading the plot for the model-predicted values, we note a non-linear dependence between these parameters with an asymptotic value $\eta = 0.25$, which is closer to the theoretical maximum (Eq. (13)) The deposition however did not hit the theoretical limit as the CFD-model accounted for the re-suspension

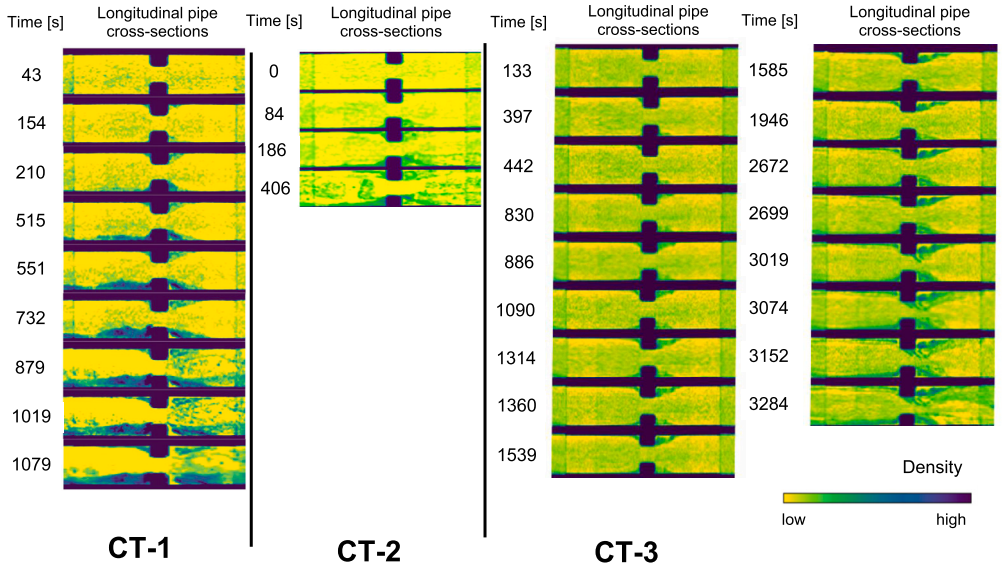

Fig. 8. Cross-section of the test section in different CT tests. Numbers represent time (s) from the start of experiments. Gravity is directed downwards, and the flow direction is from left to right. The color scale represents the material density.

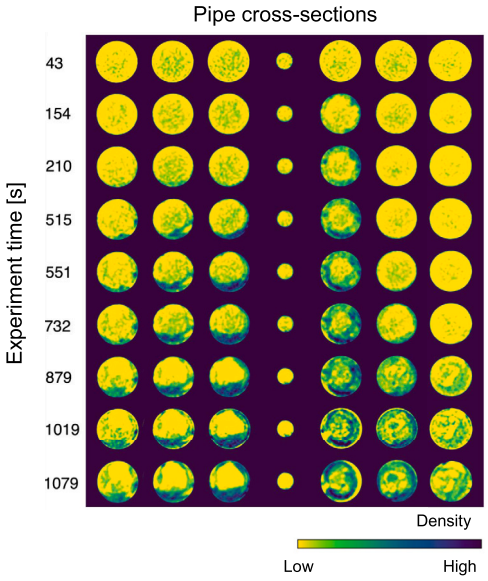

Fig. 9. CT-1: density difference in equidistant transversal cross-section. Gravity is directed downwards, and the flow direction is from left to right. The color scale represents the material density. The numbers on the left represent time from the start of the experiment (s).

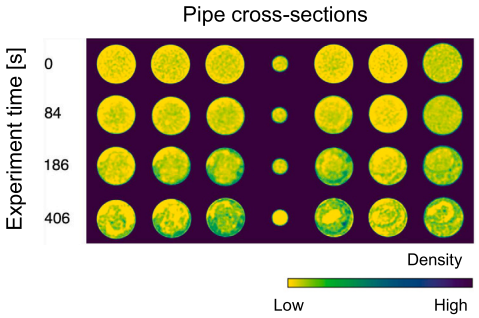

Fig. 10. CT-2: density difference in equidistant transversal cross-section. Gravity is directed downwards, and the flow direction is from left to right. The color scale represents the material density. The numbers on the left represent time from the start of the experiment (s).

of particles. The cohesive interactions of particles with the test section walls enhance the deposition and increase plugging risks. The deposition efficiency increases by about two orders when the capture probability changes from 1 to 100%. In the plot, the experimental data is averaged over time and the number of CT cases, the bottom blue line depicts the average value and the top blue line accounts for the added standard deviation. The CFD model returns values close to the experimental deposition efficiency η at $p_w \sim$ 0.4-0.5%. This low value agrees well with the order-of-magnitude estimate presented above. Therefore, we conclude that particle collisions with the frontal surface of the orifice are more important than the deposition in other parts of the test section.

Fig. 15 further illustrates the sensitivity of the model to inter-particle interactions. The deposition efficiency is presented there for a fixed p_w, but different forces acting on particles. The original CFD model (base case) is built using the methodology described in Eqs. (1)-(3), while two other versions represent cases with no account for inter-particle interactions (no interactions) and a low concentration of particles (dilute). In the first modification, we did not include the rheological expression in Eq. (2), so μ_l replaces μ_a. In addition, in the right-hand side of Eq. (3), we neglect the solid pressure force f_s, and the drag force f_d is based on a simpler Schiller-Neumann's drag coefficient (Crowe et al., 1998) with no account for a densely loaded flow. The simplified model's deposition efficiency doubles as compared to the base case. Together with the neglected inter-particle interactions, we de-couple the phases for the dilute-flow model, removing F_p from the governing equations for the liquid phase (Eq. (2)). Here, the concentration of particles also reduces to 0.9%. The resulting deposition efficiency triples compared to the base case, even considering the low probability of wall capture. We conclude that the inter-particle interactions introduce additional repulsion during the collisions and thus limit the plugging potential. Recent CFD-DEM simulations by Saparbayeva and Balakin (2023) support the conclusion. It is important to note that, in an engineering application, an increased number of particles would raise plugging risks as elevated μ_a results in higher pumping costs, which is not accounted for by the boundary conditions of our CFD model.

It is interesting to evaluate existing physical models to determine p_w. In this case, we could consider a particle moving near the settled particulate deposit. The particle is about to collide with the settled particles, and the fluid tends to prevent the collision via the drag and lift mech-

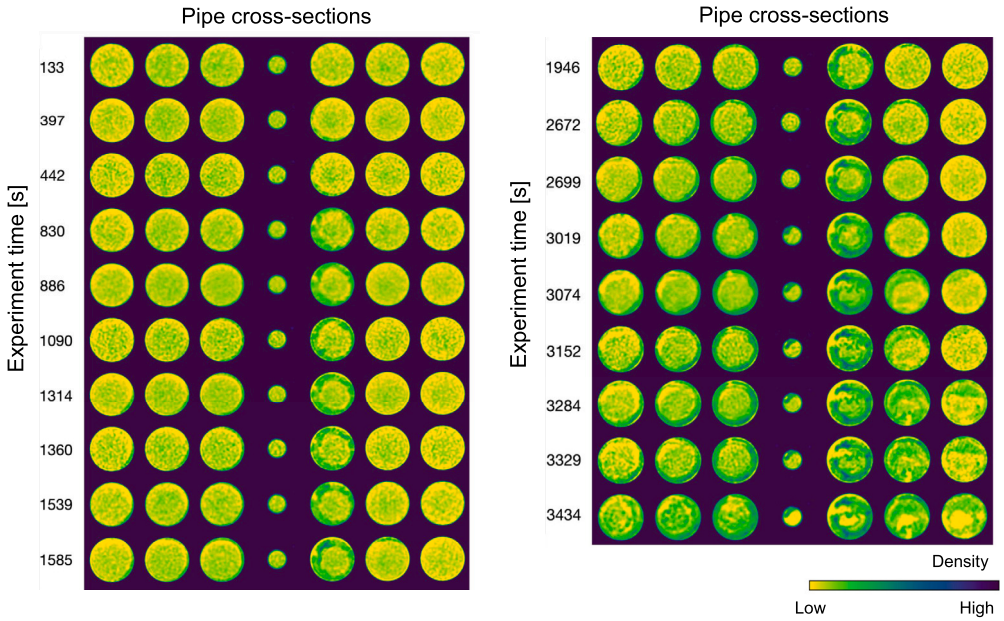

Fig. 11. CT-3: density difference in equidistant transversal cross-section. Gravity is directed downwards, and the flow direction is from left to right. The color scale represents the material density. The numbers on the left represent time from the start of the experiment (s).

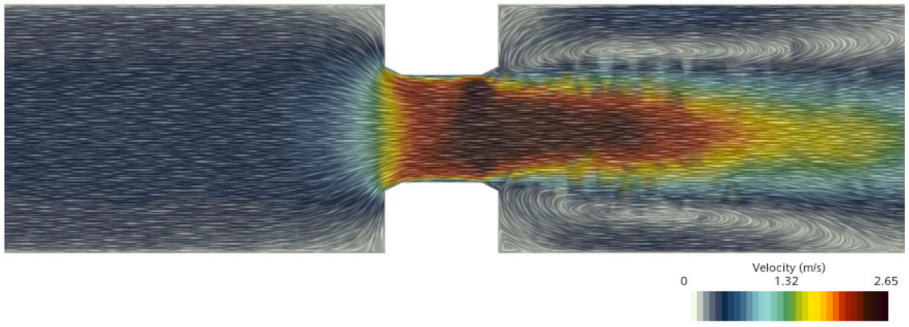

Fig. 12. Flow velocity profile predicted by the CFD model.

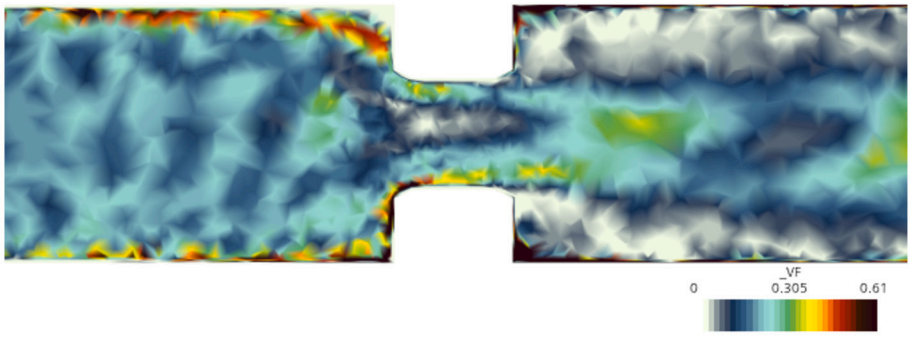

Fig. 13. Volume fraction profile predicted by the CFD model.

anisms. The cohesive forces can capture the particle within the spatial range of their significance. The particle is immersed into the laminar boundary layer, whose thickness is ∼ 900 μm in the main pipe. The theoretical analyses of particle trajectories in a shear flow by Zeichner and Schowalter (1977) provide relevant estimates for the theoretical probability p_w^{th} in such cohesive collisions:

$$p_w^{th} = 2\left(\frac{9\pi\mu_l\gamma_b d_p^3}{2A_e}\right)^{-0.25}, \tag{14}$$

where $\gamma_b = 2u/d_p$ is the shear rate in the laminar boundary layer, and u is the fluid velocity computed in the layer at the particle's mass center position. In Equation (14), A_e is the Hamaker constant as cohesion was assumed to originate from van-der-Waals interactions in the original work (Zeichner and Schowalter, 1977). We critically note that inertial particles with St∼0.12 in the laminar layer will not entirely follow the continuous phase as in the original work. In addition, according to Yang et al. (2004), ice cohesion in decane originates from capillary bridges and van-der-Waals interactions. However, we still find Eq. (14) useful for engineering estimates of the parameter, finding an effective

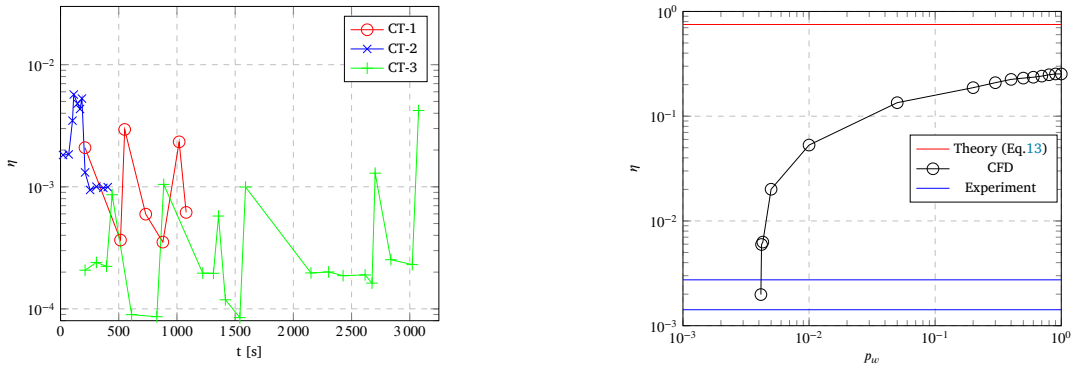

Fig. 14. Deposition efficiency. Left: experimental deposition efficiency as a function of time. Right: deposition efficiency as a function of the probability of wall capture p_w.

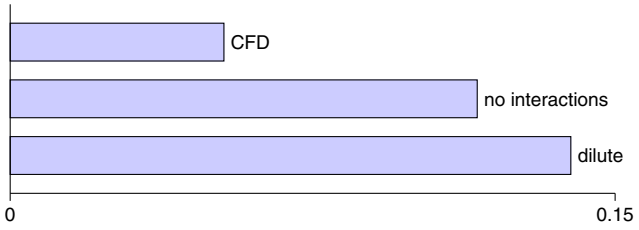

Fig. 15. Deposition efficiency η computed by: CFD-model with $p_w = 0.01$ (CFD); CFD-model with no inter-particle interactions for $p_w = 0.01$, $\mu_a = \mu_l$, $f_s = 0$ (no interactions); CFD-model for a dilute flow with $p_w = 0.01$, $\phi_p = 0.009$, $F_p = 0$ (dilute).

Hamaker constant (Israelachvili, 2011) as $A_e = 12\pi\sigma_c h_0^2$, where $\sigma_c \sim 150$ mJ/m^2 is the surface energy of ice in decane at the experimental temperatures (Yang et al., 2004), and $h_0 \sim 0.2$ nm is the cutoff distance (Israelachvili, 2011). The described method returns $p_w^{th} = (1.9 \pm 1.1)\%$ for particle sizes from 200 to 400 μm. These values are higher than the experimental ones due to the limitations of the discussed method. However, we note that the difference, which is lower than an order of magnitude, is comparable to what is often used in engineering safety factors. The theoretical analysis could be used to analyze plugging risks conservatively.

Deposited particles could re-suspend to the flow in our experiment. This would result in p_w lower than the theoretical probability p_w^{th}. We note that the condition for re-suspension from a flat surface $0.469 \cdot \sigma_c^{\frac{4}{3}} \left(\mu_l \gamma\right)^{-1} \overline{k}^{-\frac{1}{3}} d_p^{\frac{4}{3}} < 1$ (Ziskind, 2006) was not satisfied for the considered ice slurry with the stiffness of $\overline{k} = 1.5$ GPa computed with ice properties from Sukhorukov (2013) (Table 4). A more complex theoretical assessment of re-suspension requires the determination of the deposit's roughness. However, re-suspension events were observed in previous experiments (Struchalin et al., 2023) and CFD simulations (Saparbayeva and Balakin, 2023).

To quantify the influence of re-suspension, we assume that the theoretical probability is scaled with the fraction of re-suspended particles $p_w = p_w^{th} \cdot f_r$, where the latter parameter could be estimated using the empirical expression from Eskin et al. (2011):

$$f_r = 1 - \overline{\alpha}\left(\tau_w/\tau_y - 1\right)^{\overline{n}}, \tag{15}$$

where τ_w is the wall shear stress in the test section computed using the pressure drop, $\overline{\alpha} = 0.43$, $\overline{n} = 0.28$ are the empirical parameters. The yield stress in the deposit τ_y was determined following Eq.10 in the Supplementary Materials. The parameter was computed by altering particle concentration at the top of the deposit. For $\phi_p = 0.40$, 0.45, 0.50, the fraction f_r equals 0.18, 0.44, 0.73. Therefore, the wall capture probability p_w becomes (0.85±0.52)%, closer to the experimental values. This result also agrees with Fig. 15, where the CFD-model returned about twice the higher deposition efficiency for the case where the phases were uncoupled.

4. Conclusions

This article presents a combined experimental and theoretical study of plugging in the turbulent flow of cohesive ice slurries dispersed in the hydrocarbon phase. The medical CT scanner and the standard flow instrumentation simultaneously controlled the plugging experiments. The experiments depicted the main flow parameters and particle concentration profiles along the plugging process. It was found that the flow restriction in the form of the centrally open orifice, which was mounted in the test section, played a major role during the plugging. The pipeline was blocked downflow the orifice in the closest proximity of its mouth, where the wakes recycled the particles towards the pipe walls. Accounting for the elevated concentration of 15% and particle surface energy ~ 150 mJ/m^2, the process of plugging was unexpectedly long (0.5-1.0 h).

Several factors hindering plugging were identified. The CT analysis of the test section revealed the formation of sandwatch-shaped deposits uplow the orifice. These deposits streamlined the flow and limited frontal. The developed multiphase CFD model was instrumental in the more detailed physical description of the process. The simulations demonstrated that the deposition efficiency was $\sim 10^{-3}$ due to the low particle capture probability (0.4-0.5%) and the repulsive inter-particle interactions. Finally, we refer to the theories of orthokinetic coagulation and particle re-suspension to obtain estimates of the wall capture probability.

CRediT authorship contribution statement

Boris V. Balakin: Writing – original draft, Supervision, Project administration, Methodology, Investigation, Funding acquisition, Conceptualization. **Yu-Fen Chang:** Writing – original draft, Visualization, Software, Formal analysis, Data curation. **Mona Øynes:** Writing – original draft, Methodology, Investigation. **Pavel G. Struchalin:** Writing – original draft, Methodology, Investigation, Data curation.

Declaration of competing interest

The authors declare the following financial interests/personal relationships which may be considered as potential competing interests:

Boris V. Balakin reports financial support was provided by Research Council of Norway. If there are other authors, they declare that they have no known competing financial interests or personal relationships that could have appeared to influence the work reported in this paper.

Data availability

Data will be made available on request.

Acknowledgements

This project was supported by the Research Council of Norway as part of FLOWCHART project (Grant No. 300286).

Appendix A. Supplementary material

Supplementary material related to this article can be found online at https://doi.org/10.1016/j.ces.2024.120214.

References

Amin, A., 2015. Evaluation of commercially available virtual flow meters (VFMs). In: Offshore Technology Conference, OTC. pp. OTC–25764.

Balakin, B., Hoffmann, A., Kosinski, P., 2011. Experimental study and computational fluid dynamics modeling of deposition of hydrate particles in a pipeline with turbulent water flow. Chem. Eng. Sci. 66, 755–765.

Bouillard, J., Lyczkowski, R., Gidaspow, D., 1989. Porosity distributions in a fluidized bed with an immersed obstacle. AIChE J. 35, 908–922.

Crowe, C., Sommerfeld, M., Tsuji, Y., 1998. Multiphase Flow with Droplets and Particles. CRC Press.

Di Felice, R., 1994. The voidage function for fluid-particle interaction systems. Int. J. Multiph. Flow 20, 153–159.

Döppenschmidt, A., Kappl, M., Butt, H.J., 1998. Surface properties of ice studied by atomic force microscopy. J. Phys. Chem. B 102, 7813–7819.

Doron, P., Barnea, D., 1996. Flow pattern maps for solid-liquid flow in pipes. Int. J. Multiph. Flow 22, 273–283. https://doi.org/10.1016/0301-9322(95)00071-2.

Duan, X., Shi, B., Wang, J., Song, S., Liu, H., Li, X., Chen, Y., Liao, Q., Gong, J., Chen, S., et al., 2021. Simulation of the hydrate blockage process in a water-dominated system via the CFD-DEM method. J. Nat. Gas Sci. Eng. 96, 104241.

Eskin, D., Ratulowski, J., Akbarzadeh, K., Pan, S., 2011. Modelling asphaltene deposition in turbulent pipeline flows. Can. J. Chem. Eng. 89, 421–441.

George, D.L., Shollenberger, K., Torczynski, J.R., O'Hern, T.J., Ceccio, S., 2001. Three-phase material distribution measurements in a vertical flow using gamma-densitometry tomography and electrical-impedance tomography. Int. J. Multiph. Flow 27, 1903–1930.

Gillies, R., Hill, K., Mckibben, M., Shook, C., 1999. Solids transport by laminar Newtonian flows. Powder Technol. 104, 269–277.

Gillies, R.G., Schaan, J., Sumner, R.J., McKibben, M.J., Shook, C.A., 2000. Deposition velocities for Newtonian slurries in turbulent flow. Can. J. Chem. Eng. 78, 704–708.

Gosman, A., Ioannides, E., 1983. Aspects of computer simulation of liquid-fueled combustors. J. Energy 7, 482–490.

Hashemi, S., Spelay, R., Sanders, R., Hjertaker, B., 2021. A novel method to improve electrical resistance tomography measurements on slurries containing clays. Flow Meas. Instrum. 80, 101973.

Heindel, T.J., 2011. A review of X-ray flow visualization with applications to multiphase flows. J. Fluids Eng. 133, 074001.

Henry, C., Minier, J.P., Brambilla, S., 2023. Particle resuspension: challenges and perspectives for future models. Phys. Rep. 1007, 1–98.

Hirochi, T., Yamada, S., Shintate, T., Shirakashi, M., 2002. Ice/water slurry blocking phenomenon at a tube orifice. Ann. N.Y. Acad. Sci. 972, 171–176. https://doi.org/10.1111/j.1749-6632.2002.tb04569.x.

Idelchik, I.E., 2008. Handbook of Hydraulic Resistance, 4th edition revised and augmented. Begell House, Inc.

Israelachvili, J., 2011. Intermolecular and Surface Forces.

Kakitani, C., Marques, D.C., Marcelino Neto, M.A., Teixeira, A., Valim, L.S., Morales, R.E., Sum, A.K., 2019. Measurements of hydrate formation behavior in shut-in and restart conditions. Energy Fuels 33, 9457–9465.

Kauffeld, M., Kawaji, M., Egolf, P.W., 2005. Handbook on ice slurries. In: International Institute of Refrigeration, Paris, p. 359.

Kaushal, D., Tomita, Y., 2007. Experimental investigation for near-wall lift of coarser particles in slurry pipeline using γ-ray densitometer. Powder Technol. 172, 177–187.

Krupička, J., Matoušek, V., 2014. Gamma-ray-based measurement of concentration distribution in pipe flow of settling slurry: vertical profiles and tomographic maps. J. Hydrol. Hydromech. 62, 126–132.

Mondal, S., Wu, C.H., Sharma, M.M., 2016. Coupled CFD-DEM simulation of hydrodynamic bridging at constrictions. Int. J. Multiph. Flow 84, 245–263.

Muyshondt, A., McFarland, A.R., Anand, N., 1996. Deposition of aerosol particles in contraction fittings. Aerosol Sci. Technol. 24, 205–216.

Natsui, S., Ueda, S., Nogami, H., Kano, J., Inoue, R., Ariyama, T., 2012. Gas–solid flow simulation of fines clogging a packed bed using dem–cfd. Chem. Eng. Sci. 71, 274–282.

Naukanova, M., Lavalle, G., Herri, J.M., Cameirao, A., Struchalin, P.G., Balakin, B.V., 2023. Viscosity of ice-in-oil slurries. Int. J. Refrig. 150, 41–46.

Onokoko, L., Poirier, M., Galanis, N., Poncet, S., 2018. Experimental and numerical investigation of isothermal ice slurry flow. Int. J. Therm. Sci. 126, 82–95.

Poloski, A.P., Adkins, H.E., Abrefah, J., Casella, A.M., Hohimer, R.E., Nigl, F., Minette, M.J., Toth, J.J., Tingey, J.M., Yokuda, S.T., 2009. Deposition velocities of Newtonian and non-Newtonian slurries in pipelines. Technical Report. Pacific Northwest National Lab. (PNNL), Richland, WA (United States).

Rensing, P.J., Liberatore, M.W., Sum, A.K., Koh, C.A., Sloan, E.D., 2011. Viscosity and yield stresses of ice slurries formed in water-in-oil emulsions. J. Non-Newton. Fluid Mech. 166, 859–866.

Research Council of Norway, 2024. FLOWCHART. https://prosjektbanken.forskningsradet.no/en/project/FORISS/300286. (Accessed 7 April 2024). Online.

Rukhlenko, O.S., Dudchenko, O.A., Zlobina, K.E., Guria, G.T., 2015. Mathematical modeling of intravascular blood coagulation under wall shear stress. PLoS ONE 10, e0134028.

Santo, N., Kalman, H., 2017. Blinded t-bends flow patterns in pneumatic conveying systems. Powder Technol. 321, 347–354.

Saparbayeva, N., Balakin, B.V., 2023. CFD-DEM model of plugging in flow with cohesive particles. Sci. Rep. 13, 17188.

Schindelin, J., Arganda-Carreras, I., Frise, E., Kaynig, V., Longair, M., Pietzsch, T., Preibisch, S., Rueden, C., Saalfeld, S., Schmid, B., et al., 2012. Fiji: an open-source platform for biological-image analysis. Nat. Methods 9, 676–682.

Schneider, C.A., Rasband, W.S., Eliceiri, K.W., 2012. NIH image to ImageJ: 25 years of image analysis. Nat. Methods 9, 671–675.

Seeram, E., 2009. Computed Tomography: Physical Principles, Clinical Applications, and Quality Control, 3rd edition. W.B. Saunders, Philadelphia.

Shanbhag, A.G., 1994. Utilization of information measure as a means of image thresholding. CVGIP, Graph. Models Image Process. 56, 414–419.

Shuainan, Z., Qiankun, Z., Chaoqun, Y., Chen, G., 2024. Investigation of anti-clogging mechanism of ultrasound-driven oscillating slugs/bubbles and its application on continuous crystallization process. Chem. Eng. Sci. 119898.

Siemens, 2019. Somatom Perspective: Håndbok for Drifsansvarlig. Erlangen.

Siemens Digital Industries Software, 2020. Simcenter STAR-CCM+ User Guide v. 2020.1.

Silva, R.C., 2022. Experimental characterization techniques for solid-liquid slurry flows in pipelines: a review. Processes 10, 597.

Sommerfeld, M., et al., 2000. Theoretical and Experimental Modelling of Particulate Flows. Lecture Series, vol. 6, pp. 3–7.

Song, G., Li, Y., Wang, W., Jiang, K., Ye, X., Zhao, P., 2017. Investigation of hydrate plugging in natural gas+ diesel oil+ water systems using a high-pressure flow loop. Chem. Eng. Sci. 158, 480–489.

Struchalin, P.G., Balakin, B.V., 2023. Blocking dead zones to avoid plugs in pipes. Chem. Eng. Res. Des. 194, 649–952. https://doi.org/10.1016/j.cherd.2023.05.007.

Struchalin, P.G., Øye, V.H., Kosinski, P., Hoffmann, A.C., Balakin, B.V., 2023. Flow loop study of a cold and cohesive slurry. Pressure drop and formation of plugs. Fuel 332, 126061. https://doi.org/10.1016/j.fuel.2022.126061.

Sukhorukov, S., 2013. Ice-Ice and Ice-steel friction in field and in laboratory. Phd thesis. Norwegian University of Science and Technology.

Yang, S.-o., Kleehammer, D.M., Huo, Z., Sloan, E.D., Miller, K.T., 2004. Temperature dependence of particle–particle adherence forces in ice and clathrate hydrates. J. Colloid Interface Sci. 277, 335–341. https://doi.org/10.1016/j.jcis.2004.04.049.

Yang, X., Chen, S., Shi, Y., Feng, R., Cai, J., Jiang, G., 2019. CFD and DEM modelling of particles plugging in shale pores. Energy 174, 1026–1038.

Zeichner, G., Schowalter, W., 1977. Use of trajectory analysis to study stability of colloidal dispersions in flow fields. AIChE J. 23, 243–254.

Zhou, Z., Kuang, S., Chu, K., Yu, A., 2010. Discrete particle simulation of particle–fluid flow: model formulations and their applicability. J. Fluid Mech. 661, 482–510.

Ziskind, G., 2006. Particle resuspension from surfaces: revisited and re-evaluated. Rev. Chem. Eng. 22, 1–123.